Communications Biology

https://doi.org/10.1038/s42003-026-09780-y

Article in Press

Downfield magnetic resonance signals serve as endogenous imaging biomarkers of nucleotide metabolism in glioma

Received: 8 September 2025

Accepted: 19 February 2026

Cite this article as: Zhu, X., Zhou, K., Cao, Y. *et al.* Downfield magnetic resonance signals serve as endogenous imaging biomarkers of nucleotide metabolism in glioma. *Commun Biol* (2026). https://doi.org/10.1038/s42003-026-09780-y

Xinyi Zhu, Ke Zhou, Yang Cao, Jiaqiang Zhou, Yingchao Liu, Yibo Liu, Sheng Chen & Min Wang

Downfield magnetic resonance signals serve as endogenous imaging biomarkers of nucleotide metabolism in glioma

Xinyi Zhu[1], Ke Zhou[1], Yang Cao[1], Jiaqiang Zhou[2], Yingchao Liu[3], Yibo Liu[4], Sheng Chen[4], Min Wang[1,2*]

[1]Key Laboratory for Biomedical Engineering of Ministry of Education, College of Biomedical Engineering and Instrument Science, Zhejiang University, Hangzhou, Zhejiang, China

[2]Department of Endocrinology and Metabolism, Sir Run Run Shaw Hospital, Department of Endocrinology, Zhejiang University, Hangzhou, China

[3]Department of Neurosurgery, Shandong Provincial Hospital Affiliated to Shandong First Medical University, Jinan, China

[4]Department of Neurosurgery, School of Medicine, The Second Affiliated Hospital, Zhejiang University, Hangzhou, China

[*]Correspondence to:

Min Wang, Zhou Yi Qing Building, No.38 Zheda Road, Hangzhou, Zhejiang, 310027, China; Phone: 86-183-68154967; E-mail: wangmin707@zju.edu.cn.

Abstract

Gliomas, the most common primary brain tumors, exhibit profound metabolic alterations that can be non-invasively probed using magnetic resonance spectroscopy (MRS). Compared to upfield signals in traditional MRS, downfield signals exhibit complex composition with limited understanding of their metabolite origins. Correlating high-throughput metabolic profiles provided by untargeted metabolomics with MRS signals can help elucidate the origins of metabolites in MRS. In this study, upfield and downfield MRS spectra are obtained from control and glioma-bearing male Wistar rats, followed by correlation analysis with untargeted metabolomics from corresponding brain tissues. Here, we show that multiple downfield MRS peaks are significantly elevated in glioma rats and correlate with metabolomic features. Notably, downfield MRS demonstrate the capability of capturing adenosine triphosphate (ATP)-associated nucleotide metabolism. Furthermore, MRS signatures exhibit predictive potential for tumor growth parameters. This work establishes an integrated MRS-metabolomics framework, providing a basis for non-invasively monitoring dynamic metabolic reprogramming and predicting glioma progression.

Introduction

Glioma is one of the most common primary malignant tumors of the central nervous system, accounting for approximately 49%[1, 2]. Given its high prevalence, precise diagnosis for glioma is critical for effective clinical management. Although molecular subtyping advances tumor classification[3, 4], the rapid progression of tumor necessitates non-invasive tools to monitor dynamic metabolic states, which are crucial for assessing metabolic reprogramming and treatment.

MRS provides a non-invasive technique to measure the resonance peaks of protons from different metabolic molecules based on chemical shifts. Traditionally, MRS typically focuses on upfield signals (0~4 ppm), where higher metabolite concentrations are readily detectable and widely used for tumor evaluation. In contrast, the downfield region (6~10 ppm) remains challenging to detect due to rapid proton exchange with water and lower metabolite concentrations[5] and is often overlooked[6, 7]. Nevertheless, this spectral region was reported to contain signals from potential metabolites such as ATP, whose pivotal role in cellular energetics makes it a potential theranostic target[8], along with homocarnosine, protein amide, tyrosine[6, 7]. Altered downfield phenylalanine resonance was also observed in phenylketonuria patients[9]. These insights, which are inaccessible in conventional upfield MRS, make the simultaneous detection of both upfield and downfield signals essential for a more comprehensive tumor MRS profile.

Technical innovations have been developed to detect downfield signals. Recently, non-water-saturation techniques have been suggested to capture the full downfield signal intensity[10]. For instance, metabolite-cycling (MC) methods have been applied to study the physical properties of downfield signals[7, 11], and image-selected in vivo spectroscopy (ISIS)[10] combined with selective excitation has been used for single-voxel downfield spectroscopy in glioma-bearing mice[12]. Furthermore, spectral-spatial selective excitation pulses combined with magnetic resonance spectroscopic imaging (MRSI) improve acquisition efficiency, enabling the measurement of the spatial distribution of downfield MRS signals[13, 14]. Despite these advancements in signal detection, downfield signals still face challenges: (1) the spectral complexity and peak overlap hinder the precise interpretation of metabolic signatures, which consequently limits

clinical applications[12], and (2) the signal composition could vary significantly across different TEs, as suggested by previous studies[15]. Meanwhile, upfield analysis is also confounded by overlapping signals from macromolecules and mobile lipids, particularly at short TE[16]. Thus, investigating both the upfield and downfield MRS signal compositions is critically needed for non-invasive interpretation of tumor metabolism.

To address these analytical challenges in MRS, untargeted metabolomics, with its ability to measure all detectable metabolites within a tissue, provides a molecular level reference. This technique is known to reveal tumor-specific metabolic profiles by sensitively detecting various small-molecule metabolites[17, 18, 19]. For example, 2-hydroxyglutarate (2-HG)[20] has been identified as highly specific in IDH-mutant gliomas, serving as a key diagnostic indicator. By correlating the macroscopic metabolic landscape from in vivo MRS with the microscopic molecular details from untargeted metabolomics, we aim to further elucidate the metabolic origins of MRS, especially for downfield signals.

Predicting tumor progression is as crucial as diagnosis, offering valuable insights into tumor biology. While tumor size informs staging and correlates with survival[21], the tumor growth rate (TGR) is a critical indicator of tumor aggressiveness, as rapidly growing tumors often exhibit increased invasiveness and treatment resistance. Consequently, this study also explores the associations between MRS and metabolomics features with tumor growth dynamics to evaluate this metabolic information as non-invasive biomarkers for predicting tumor progression.

In summary, this study aims to: (1) simultaneously acquire upfield and downfield MRS signals with a metabolic-cycling PRESS (MC-PRESS) at two TEs; (2) correlate MRS signals with untargeted metabolomics data from corresponding tissues to elucidate the origins of MRS spectra; (3) evaluate the associations of these metabolic features with tumor growth dynamics (tumor size and TGR). Our integrated analysis demonstrates a strong correlation between several downfield MRS signals and nucleotide metabolites in the ATP metabolic pathway. Furthermore, MRS signals also correlate with tumor growth parameters, highlighting their potential as non-invasive biomarkers for predicting tumor progression.

Results

Upfield and downfield MRS: in situ metabolism dysregulation in glioma

As shown in Fig. 1a, MRS spectra were acquired at TE of 6.9 ms and 15 ms from C6 glioma rat models (tumor-bearing group, TB) and healthy control rats (HC). Based on longitudinal monitoring of tumor size and morphology[22], the TB group was subdivided into early-stage (ES) and late-stage (LS) glioma. Representative spectra (Fig. 1b) and normalized average spectra (Fig. 1c) within each of the three groups were presented. The MRS spectra from normal and tumor tissues showed similar inter-group differences with previous studies[12, 23].

Statistical analysis revealed progressive changes in MRS signals during tumor progression (Fig. 2). For upfield signals (Fig. 2a), glutathione (GSH), inositol (Ins), lactate (Lac), and tCh levels increased in the LS group at both TEs; whereas N-acetylaspartate (NAA), glutamate (Glu), and glutamine (Gln) were gradually reduced during tumor progression at both TEs. And taurine (Tau) increased in the LS group compared to HC only at TE = 15 ms. tCr and γ-aminobutyric acid (GABA) showed no statistically significant difference between groups at either TE. The coefficients of variation (CV) for tCr signals within the three groups were 20.4%, 20.0%, and 15.5% at TE = 6.9 ms, and 20.1%, 27.1%, and 23.6% at TE = 15 ms, respectively.

For downfield signals (Fig. 2b), DF6.83 and DF7.09 were significantly elevated in the TB group at both TEs. DF8.18, DF8.37, and DF8.x showed increasing trends with tumor progression only at TE = 6.9 ms, whereas DF7.30 and DF8.49 were higher in the TB group compared to the HC group only at TE = 15 ms. All downfield signals showed marked decay with increasing TE in the three groups, with all average decay ratio > 20% (Supplementary Table 1). The total sum of the downfield signals (Fig. 2c, d) in the tumor was higher than in normal tissue at both TEs.

Water signals (Fig. 2e, f) significantly increased in tumor at both TEs. The correlation between water signal and metabolite signals were summarized in Supplementary Table 2. Several upfield and downfield

signals in HC group exhibited significant correlation with water, while this correlation were mostly disrupted in the ES and LS groups.

Untargeted metabolomics: metabolic reprogramming in glioma

Tissue samples were extracted based on MRS voxel locations and further analysed via liquid chromatography with tandem mass spectrometry (LC-MS/MS). A total of 1625 metabolites were identified (Fig. 3a), and the heatmap of hierarchical clustering analysis illustrated distinct metabolic differences between tumor and normal tissues. Among the identified metabolites, 180 with unknown classification were excluded, resulting in a total of 1,445 metabolites over 12 classes (Fig. 3b). Principal component analysis (PCA) and orthogonal projections to latent structures-discriminant analysis (OPLS-DA) effectively separated tumor from metabolomics profiles of normal brain tissues (Fig. 3c-d). The OPLS-DA model did not overfit according to random permutation tests (Fig. 3e). Compared to normal tissues, tumor tissues showed 380 significantly upregulated and 312 significantly downregulated metabolites (Fig. 3f). As shown in Fig. 3g, the top-ranked downregulated metabolites included phosphatidylcholine (22:2), N-acetyl aspartic acid, and γ-aminobutyric acid (GABA), while the top-ranked upregulated metabolites included deoxycytidine and acetic acid in tumor tissues.

As depicted in Fig. 4a, PCA was applied to each metabolite class with sufficient members ($n > 12$). Principal components (PCs) were selected using a 90% explained variance threshold, and the resulting PCs were then tested for their ability to differentiate between normal and tumor groups (Fig. 4b). The first PC significantly discriminated between normal and tumor tissues across most metabolite categories, with the most pronounced differences ($P \leq 0.001$) in nucleotides, benzenoids, and lipids, indicating marked alterations in their metabolic network activity in tumor tissues.

Correlations of MRS and untargeted metabolomics: global metabolic alterations and specific metabolites origins

The overall correlation patterns between MRS signals and untargeted metabolomics metabolites were presented in Figure 5. The cosine similarity of overall correlation patterns between two TEs was 0.8026 for upfield signals (Fig. 5a) and 0.3077 for downfield signals (Fig. 5b). Correlation coefficient difference matrices (Fig. 5c) further interpreted the differences in correlation distributions between the two TEs. Supplementary Table 3 presented the cosine similarity for each MRS peak's correlation patterns across TEs. Notably, upfield NAA, tCr, tCh, Lac, and Glu showed high pattern consistency (cosine similarity > 0.9), while only downfield DF7.09 showed high pattern consistency.

Based on the PCs and their eigenvalues derived from metabolomics data, the composite PCA score vector for each metabolomics category was calculated, and the correlations between this composite vector and MRS signals were then evaluated. For upfield signals (Fig. 6a), NAA, Glu, and Gln showed negative correlation with nucleotides and benzenoids. In addition, tCh, Lac, Ins, GSH, and GABA exhibited similar correlation distributions, showing positive correlation with benzenoids while negatively correlating with organic acids and lipids. Downfield signals exhibited TE-specific correlation profiles (Fig. 6b). Crucially, at TE = 6.9 ms, DF7.09, DF7.30, DF8.18 and DF8.x exhibited positive correlations with nucleotides, and DF6.83, DF7.09, DF7.30 and DF8.x exhibited positive correlations with benzenoids; While at TE = 15 ms, DF8.49 was positively correlated with benzenoids. Based on correlation distribution (Fig. 5b), probability densities were calculated for correlations between metabolite classes and each downfield signal (Supplementary Figure 1). The integrated density for strong correlations ($r > 0.7$) was quantified (Fig. 6c). At TE = 6.9 ms, nucleotides showed a high probability (probability density > 0.24) of strong positive correlations with DF6.83, DF8.18, and DF8.x, while no such strong correlations were observed at TE = 15 ms.

Table 1 systematically summarized the correlation analysis between MRS signals and their known/suspected corresponding specific omics-derived metabolites to explore specific metabolite-spectral linkages. Significant positive correlations were observed between upfield Glu and NAA and their corresponding omics-derived metabolites at both TEs, whereas Gln, tCr, and GABA demonstrated stronger correlations at TE = 15 ms compared to TE = 6.9 ms. While for downfield MRS signals, at TE = 6.9 ms,

several ATP downstream products, including xanthine, uric acid, deoxyadenosine, deoxyinosine, and ribose-1-phosphate showed positive correlations with DF6.83. Moreover, uric acid, deoxyadenosine, and deoxyinosine were positively correlated with DF8.18. At TE = 15 ms, xanthine, uric acid, deoxyadenosine, and deoxyinosine exhibited positive correlations with DF8.49, deoxyadenosine and deoxyinosine were additionally correlated with DF6.83. Besides, GSH showed a correlation with DF7.09 at TE = 15 ms.

Correlations of MRS and tumor growth parameters: metabolic-morphological linkage

As illustrated in Fig. 7a, longitudinal anatomical images acquired during tumor progression were used to calculate tumor volumes for all TB rats. The TGR for each rat (Fig. 7b) was then fitted using longitudinal tumor volume data collected at multiple time points. The correlations between all MRS signals and either tumor size or TGR were summarized in Supplementary Table 4. Tumor size was positively correlated with upfield Ins and Lac, while negatively correlated with NAA and Gln at both TEs. Additionally, GSH showed a positive correlation with tumor size at TE = 6.9 ms. Furthermore, tumor size also exhibited a positive correlation with DF8.18 and a negative correlation with DF8.24 at TE = 6.9 ms (Fig. 7d). Regarding TGR (Fig. 7e), at TE = 6.9 ms, TGR was positively correlated with GSH; while at TE = 15 ms, TGR demonstrated positive correlations with Ins, Tau, DF8.18, and DF8.x.

Discussion

Downfield MRS signals can provide unique metabolite information that cannot be detected in upfield MRS, thus holding promise for complementing conventional upfield biomarkers in neuro-oncology[12, 24]. However, their metabolite origins are still areas of active research, and there is a lack of research exploring the relationship between in vivo MRS signals and ex vivo metabolomics, or their relationship to tumor growth. Here, we systematically correlated in vivo MRS signals with ex vivo untargeted metabolomics and revealed the potential of downfield signals to characterize nucleotide metabolism and provided support for the metabolic compositions of both upfield and downfield signals. Building on biochemical insights, the

correlation between MRS signals and tumor growth dynamics further deepens our metabolic understanding of tumor development and invasion.

MRS signals revealed distinct metabolism patterns between normal and tumor tissues. Notably, the TEs used were much shorter than the T2 relaxation time of upfield signals, thus no significant decay was observed. In contrast, downfield signals have significantly shorter apparent T2 relaxation times due to rapid exchange with water, resulting in noticeable signal decay. Thus, previous studies emphasized the use of short TE to minimize downfield signal loss and maximize signal-to-noise ratio (SNR)[10, 13, 15]. Furthermore, we systematically evaluate several potential factors to ensure the reliability of our SNR-based comparison: First, the observed metabolic differences are unlikely to be driven by variations in water, as the correlation between the water signal and multiple metabolite signals were observed in HC but were absent in tumors. This linkage in normal tissue may suggest an underlying physiological covariation[25], whereas its absence in tumors likely indicates disruption by tumor-specific biological processes, such as metabolic reprogramming and liquefactive necrosis. Additionally, while macroscopic B0 homogeneity was comparable across groups (Supplementary Figure 4), tumor heterogeneity can still affect locally induced magnetic fields and intrinsic T2 relaxation[26], thereby increasing linewidth (Supplementary Figure 3). Moreover, the general lack of correlation between metabolite linewidth and SNR (Supplementary Table 7) suggests that spectral broadening had limited impact on our SNR-based comparisons. The observed negative correlation for NAA in LS tumor likely reflects the co-occurrence of neuronal loss and increased tissue heterogeneity. Finally, the consistency between our SNR-based analysis and the results derived from tCr-referenced metabolite ratios (Supplementary Figure 2) further ensure the reliability of our methodological approach.

Untargeted metabolomics revealed extensive reprogramming in tumor tissues. The upregulated metabolites including deoxycytidine (related to nucleotide metabolism, promoting DNA synthesis), acetic acid, and propanoic acid indicated tumor metabolic reprogramming; conversely, decreased levels of NAA, GABA, and specific amino acids suggested impaired neuronal function and metabolic pathways, consistent with the displacement of normal brain parenchyma by tumor tissue. Additionally, PCA based on metabolite

categories demonstrated significant alterations in nucleotides, benzenoids, and lipid metabolism. These shifts reflect important tumor metabolism reprogramming: Lipids are known to play crucial roles in promoting tumor growth and regulating cell death[27, 28]; Nucleotide metabolism is commonly upregulated in human cancers[29] to support uncontrolled proliferation and immune evasion, and nucleotide synthesis inhibitors are also backbones of therapy for many cancer indications[30]; Benzenoids, such as hippuric acid from purine degradation, also exacerbate brain tissue damage due to potential neurotoxicity[31].

Upfield MRS resonances of NAA and Glu showed significant correlations with their corresponding metabolomics metabolites. Enhanced correlations for some metabolites (Gln/tCr/GABA) at TE=15 ms likely resulted from macromolecule signal decay, improving baseline fitting and quantification accuracy [32]. The lack of correlation for other metabolites may due to signal overlap, for instance, the lactate MRS signal overlaps with macromolecule (MM)[33] and lipid signals[34].

The downfield signals DF6.83 and DF8.18 at TE = 6.9 ms were specifically correlated with metabolites in the ATP pathway. Although ATP itself is highly unstable and has been reported to be rapidly consumed in ex vivo glioblastoma samples[35], its downstream products showed significant correlations. This is chemically plausible, as the adenine moiety of ATP produces signals at ~8.2 ppm and 8.51 ppm[24], and its amino group resonates at 6.755 ppm[36]. From a physiological perspective, cells are known to maintain high intracellular levels of adenine-based nucleotides, releasing ATP at rest[37], and the concentration of ATP in the normal brain is ~3mM[37]. Dysregulated cancer cell growth is largely driven by altered mitochondrial energy production[38], and tumor-associated cells in glioblastoma are reported to have enhanced mitochondrial activity and increased ATP to promote tumor growth and invasion[39]. These evidences collectively imply the contribution of ATP to downfield signals.

To evaluate other potential contributors to the downfield signals, we examined metabolites previously associated with the ~8.2 ppm region, such as GSH and amide protons. In our study, oxidized GSH products did not show a significant correlation with DF8.18 but instead exhibited a correlative trend with DF7.09 at TE = 15 ms, which suggests DF7.09 may better reflect GSH metabolism. This aligns with the reported resonance of the glycine NH group in GSH at 7.15 ppm[32], while the lack of significant correlation at TE =

6.9 ms can be explained by overlap with homocarnosine (7.1 ppm)[36]. Additionally, amide protons are widely distributed in protein and peptide backbones and are closely associated with organic acids within the untargeted metabolomics categories. However, our study found no correlation other than nucleotides and aromatic compounds with DF8.18 (Figure 6). And most free amino acids were also not correlated with DF8.18 (Supplementary Table 5). Notably, an independent study combining chemical exchange saturation transfer (CEST) and MRS[40] further support our interpretation. This work demonstrated that downfield saturation effects persist at a relatively long TE (45 ms) at 3T. Considering the rapid exchange of amide protons, they attributed it to the potential contribution of ATP, which exchanges with water through Nuclear Overhauser Effect (NOE).

The impact of different sequence acquisition methods on downfield signal composition is also noteworthy. Specifically, the MC method yielded relatively lower intensity of DF8.x peaks[7, 10, 41] compared to selective excitation/refocusing methods[10, 12, 42]. Notably, the selective excitation/refocusing method maximizes signals with rapid water exchange (e.g., DF8.x) by maintaining the water proton pool near thermal equilibrium, a mechanism known as longitudinal relaxation enhancement (LRE) effect[43, 44]. However, in the MC method, the non-selective excitation pulse drives the entire water proton away from thermal equilibrium, potentially resulting in a less pronounced LRE effect[45]. Furthermore, the exchange with water protons in the transverse magnetization could also lead to a shorter apparent T2 for the DF signals[7], thereby accelerating the decay of DF8.x. Additionally, the delay between the inversion pulse and the excitation pulse in the MC method could also contribute to a minor signal reduction[23]. The above methodological differences are critical for interpreting the downfield signals. Since amide protons exchange more rapidly with water (10-300 s^{-1})[46] than the C-H protons on the purine ring of ATP, signals from amide protons with fast exchange can be attenuated in the MC method. Consequently, the slow-exchangeable protons within ATP likely contribute more to DF8.x. This mechanism is self-consistent with our observed significant correlation between DF8.18 and downstream ATP metabolites. Therefore, the potential influence of sequence design must be explicitly considered when comparing downfield spectra across

studies, and future studies comparing the performance of these two methods in detecting downfield signals will be of great significance.

Although C6 cells are consistently used for tumor modeling to ensure genetic and cell line consistency, tumor size and TGR varied among rats, likely due to individual immune responses and tumor microenvironments. Nevertheless, all tumors exhibited the progressive growth patterns and invasion characteristic of C6 cell-induced tumors, similar to human tumors[47, 48]. The significant decrease in NAA signal with increasing tumor size indicates progressive neuronal damage during tumor growth. Meanwhile, the correlation between both lactate MRS signals and metabolomics data with tumor size (Supplementary Table 6) suggests sustained activation of anaerobic glycolysis within the tumor microenvironment. In addition, the strong correlation between Ins with TGR revealed its important role in tumor progression, as evidence suggesting upregulated de novo inositol synthesis to promote cell proliferation in cancer[49].

Several limitations of this study should be acknowledged. First, LC–MS/MS metabolite detection can be complicated by differences in ionization efficiency and fragmentation behaviour[50, 51], more mechanistic studies are needed to establish causality of our findings. Subsequent studies using high-resolution magic angle spinning (HRMAS) solid-state nuclear magnetic resonance (NMR) or targeted metabolomics could provide complementary validation for the MRS-metabolomics associations. A recent study successfully correlated biochemical changes in mouse brain tissue with plasma profiles using HRMAS[52], also highlighting the broad potential of multidimensional NMR techniques. Clearly, larger sample sizes are needed to improve the statistical power and reliability of omics analysis. Second, the MRS SNR values in this study were not corrected for relaxation times and therefore cannot be directly equated to absolute concentrations. Given that the TEs used were much shorter than the transverse relaxation time of upfield metabolite signals (>120 ms at 7T)[53], we suggest that T2 have little impact on the upfield signal. Considering the limited research on T2 relaxation times of downfield signals in tumor tissues, future studies comparing DF signals in normal and tumor tissues would be meaningful. Furthermore, future studies could detect downfield signals changes across tumor types and neuropsychiatric disorders[54], and explore their correlations with critical clinical indicators such as recurrence, survival, and treatment efficacy.

In conclusion, by applying the MC-PRESS sequence, our integrated analysis establishes a direct link between in vivo MRS and the ex vivo untargeted metabolomic of glioma and normal brains. Specifically, downfield signals, particularly DF6.83 and DF8.18, show promise as endogenous molecular imaging markers for metabolic changes in nucleotide metabolism, particularly ATP. MRS signals also demonstrate potential for non-invasively monitoring dynamic tumor metabolic turnovers. Collectively, these findings advance the biological interpretation of MRS signals while establishing guidance for their clinical application in precise neuro-oncology, with promising prospects for extending this methodology to other diseases.

Methods

Animal model preparation

All animal procedures were approved by the Animal Ethics Committee of Wenzhou Medical University (Experimental Animal Center, Wenzhou Medical University; approval number: wydw2024-0564). We have complied with all relevant ethical regulations for animal use. Thirteen male Wistar rats (~300 grams, 8-10 weeks old) were divided into two groups (TB group: n = 7 and HC group: n = 6). All TB group rats were immobilized and anesthetized by intraperitoneal injection of 5 mL/kg of 10% chloral hydrate. Based on the brain atlas, the drilling site was determined (AP: 1 mm; ML: 2.5 mm; DV: 5 mm), $1\times10^{\wedge6}$ C6 glioma cells were injected into the rat brain using a 10 μL gastight syringe with an injection rate of 2 μL/min. After the injection, the needle was left in place for 5 minutes, then slowly retracted. The burr hole was sealed with bone wax, the wound sutured and disinfected, and the rats returned to their cages for normal care after regaining consciousness. After surgery, the rats' recovery time, behavioural status, food intake, and activity levels were monitored over the next 24 hours to ensure normal conditions. After 10 days post-surgery, all tumor-bearing rats were scanned with MRI at a 3-day interval to monitor the tumor growth.

MR data acquisition

Experiments were performed using a 7T Bruker BioSpin MRI GmbH scanner, equipped with 570 mT/m gradients. A dual-channel transmit coil and a single-channel surface coil were used for signal transmission and reception. Spectroscopy data were acquired approximately 3-5 weeks after tumor cell injection. The rats anesthetized with 1.5% isoflurane were scanned. The anatomical T_2-weighted (T_2W) images of the rat brain were acquired with a RARE sequence (TE/TR = 8.8/3398 ms, FOV = 3.5 × 3.2 cm^2, matrix size = 256 × 256, and 0.75-mm slice thickness). Throughout the scan, anaesthesia was maintained via a face mask at a concentration of 1-2% isoflurane, maintaining the rats' respiratory rate at 80-90 BPM, while the ambient temperature was stabilised at 37 $^{\circ}$C. B0 shimming was performed before MRS acquisition, and a B0 field map was acquired. A voxel mask corresponding to the MRS voxel was applied to extract B0 values within the voxel, and the standard deviation of the within-voxel B0 map (B0_std) was calculated. The B0_std was comparable across groups (Supplementary Figure 4), and the mean linewidth of the water signals across all three groups was below 16 Hz (Supplementary Table 8). The MC-PRESS sequence was used to acquire single-voxel MRS data. This sequence employed the metabolite-cycling method[7] by applying inversion pulses before PRESS localization excitation. The parameters for MC-PRESS were as follows: TR = 6000 ms, two TEs of 6.9 ms and 15 ms, excitation bandwidth = 5000 Hz. Notably, TE = 6.9 ms represents the shortest achievable TE for this sequence, maximizing the SNR of downfield signals. TE = 15 ms was chosen to be comparable with previous studies of downfield signals. The inversion pulse was a hyperbolic secant adiabatic pulse to ensure stable slice profiles and alternately flips the upfield and downfield signals. The inversion pulse bandwidth was 2000 Hz, with its centre frequency alternately set to 0.5 ppm and 8.9 ppm, targeting the upfield and downfield signals, respectively. In addition, outer volume suppression (OVS) modules were implemented to improve localization accuracy. A total of 120 averages were acquired over 12 minutes. For HC rats, the voxel was placed in the right hemisphere of the brain, centered at the tumor injection point, while for tumor rats, tumor voxel sizes were adjusted according to tumor morphology to encompass the majority of the parenchyma region, and the voxel size is around 41.25-165 μL. All MR data were collected from tumor rats between day 17 and day 35 post-injection. Based on tumor growth size and upfield MRS signals, the tumor group was further divided into ES tumor group

(tumor size = 19.26 ± 9.80 mL, tCr/NAA = 0.97 ± 0.06) and LS tumor group (tumor size = 188.71 ± 96.31 mL, tCr/NAA = 1.91 ± 0.66) tumor groups[22]. For comparison, the tCr/NAA ratio in HC was 0.89 ± 0.11.

Sample preparation and untargeted metabolomics profiling

Tissue extraction was performed within one hour after MRS scanning, following anaesthesia and perfusion. Sampling location and size were aligned with MRS voxel positions, and samples were stored at -80 °C for analysis. 25 mg of each sample was weighed at low temperature into an EP tube, and 500 μL of extraction solution (methanol: acetonitrile: water = 2:2:1) was added. After vortexing for 30 s, the mixture was homogenized using a homogenizer (35 Hz, 4 min) and then sonicated on ice for 5 min. The homogenization and sonication cycle were repeated three times. The samples were incubated at -40 °C for 1 h and centrifuged at 12,000 rpm at 4 °C for 15 min. The supernatant was then transferred to a vial for instrument analysis.

LC–MS/MS analyses were performed using a UHPLC system (Vanquish, Thermo Fisher Scientific) and a Waters ACQUITY UPLC BEH Amide (2.1 mm × 50 mm, 1.7 μm)[55] coupled to Orbitrap Exploris 120 mass spectrometer (Orbitrap MS, Thermo). The mobile phase consisted of 25 mmol/L ammonium acetate and 25 mmol/L ammonia hydroxides in water (pH = 9.75) (A) and acetonitrile (B). The auto-sampler temperature was 4 ℃, and the injection volume was 2 μL. The Orbitrap Exploris 120 mass spectrometer was used for its ability to acquire MS/MS spectra on information-dependent acquisition (IDA) mode in the control of the acquisition software (Xcalibur, Thermo). In this mode, the acquisition software continuously evaluates the full scan MS spectrum. The ESI source conditions were set as following: sheath gas flow rate as 50 Arb, Aux gas flow rate as 15 Arb, capillary temperature 320 ℃, full MS resolution as 60000, MS/MS resolution as 15000, collision energy: SNCE 20/30/40, spray voltage as 3.8 kV (positive) or -3.4 kV (negative), respectively.

ProteoWizard was used to convert the raw data to the mzXML format, and peak detection, extraction, alignment, and integration were performed using R based on XCMS. The R package and the BiotreeDB (V3.0) were applied in metabolite identification[56], metabolites were identified according to the

Metabolomics Standards Initiative (MSI)[57], the identified metabolites matched the retention time (RT), precursor ion m/z (MS1), and product ion m/z (MS2). Metabolites were classified according to the Human Metabolome Database (HMDB)[58]. In this study, a total of 38518 peaks were detected and 1625 metabolites were left after relative standard deviation de-noising. Then, the missing values were filled with half of the minimum value. Also, the internal standard normalization method was applied to the raw data. Following preprocessing, Z-score normalization was performed on the sample data, and hierarchical clustering heatmap analysis was conducted to evaluate the overall metabolic differences between normal and tumor tissues. SIMCA software (V18.0.1, Sartorius Stedim Data Analytics AB, Umea, Sweden) was used to perform multivariate analysis. Data was logarithmically transformed to minimize the impact of both noise and high variance of the variables. PCA was carried out to visualize the distribution and grouping of the samples[59]. OPLS-DA[60] was then applied to visualize group separation and find significantly changed metabolites. The permutation test established 200 OPLS models by randomly changing the order of the categorical variables Y to obtain the R2 and Q2 values of the stochastic model. Furthermore, the values of variable importance in the projection (VIP) of the first principal component in OPLS-DA analysis were obtained. The metabolites with VIP > 1 and $P < 0.05$ were considered as significantly differential metabolites. The top 10 significantly upregulated and top 10 significantly downregulated metabolites were selected based on P significance and visualized using a heatmap, and hierarchical clustering of the top differentially expressed metabolites was performed using the complete linkage method.

For each metabolomics category, PCA was performed using the built-in sklearn package in Python. Specifically, for a single-class metabolomics dataset $D_{n\times m}$, where n represents the number of tissue samples and m represents the number of metabolites in an individual metabolomics category. PCA was applied to obtain the eigenvector matrix $U_{m\times m}$ and eigenvalue matrix $V_{m\times 1}$. Based on a threshold of no more than 90% of the total explained variance, the eigenvector matrix $U'_{m\times k}$ ($k < m$) and eigenvalue matrix $V'_{k\times 1}$ were obtained. The PCA score matrix $P_{n\times k}$ was computed according to equation (1):

$$P_{n\times k} = D_{n\times m} \times U'_{m\times k} \quad (1)$$

$P(i, j) \in n \times k$ denoted the PCA score of sample i across the j principal components.

Eigenvalue-weighted feature vector $E'_{m\times 1}$ for each metabolite category was calculated using equation (2) to represent its overall metabolic variation:

$$E'_{m\times 1} = U'_{m\times k} \times V'_{k\times 1} \quad (2)$$

Subsequently, by projecting all samples onto the eigenvalue-weighted feature vector using Equation (3), the composite PCA score vector $P'_{n\times 1}$ within each metabolite category were obtained:

$$P'_{n\times 1} = D_{n\times m} \times E'_{m\times 1} \quad (3)$$

Metabolites listed in Table 1 met the following inclusion criteria: For upfield signals, the metabolite origins are relatively well-established, thus the corresponding metabolites identified through metabolomics were selected. It should be noted that NAA and GSH are unstable ex vivo; therefore, their respective metabolic derivatives — aspartate (breakdown product of NAA) and glutathione disulfide (GSSG, oxidation product of GSH) — were used as ex vivo markers. PCr is also unstable and has been reported to be rapidly consumed in ex vivo glioblastoma samples[35], therefore, only the correlation between creatine and tCr MRS signal was calculated. For downfield signals, since their metabolite attribution is primarily based on theoretical speculation, potential contributors such as NAA, glutathione, ATP, phenylalanine, histidine, Gln, tryptophan, and tyrosine, as reported in prior literature[24], were included. Considering the instability of ATP under ex vivo conditions and its undetectability via direct measurement, analysis was performed on the downfield resonances associated with its sequential degradation products (Supplementary Figure 5).

MR data processing

The MRS spectra were processed using the MATLAB FID-A toolbox. After coil combination and zero-filling, frequency and phase alignment were performed using the water peak. A correction factor was calculated from the first 16 points FID signals[61] to minimize water sideband errors. During acquisition, the

upfield and downfield signals were alternately flipped, thus summing the flipped signals yielded the water spectrum, while subtracting them yielded the upfield and downfield spectra.

Water signals were fitted by AMARES using a Lorentzian shape in JMRUI. Metabolite spectra were fitted using LCModel[62], as shown in Supplementary Figure 6. Upfield signals were fitted between 0 and 4.2 ppm using a simulated basis set[63] consisting of 16 metabolites, with tCh as the sum of glycerophosphorylcholine and phosphorylcholine, and tCr as the sum of creatine and phosphocreatine. Macromolecule and background fitting was performed with default LCModel settings, using built-in splines[64]. The fitting errors of the overlapping signals were evaluated using Cramér-Rao lower bounds (CRLBs). The fitting results of upfield signals with CRLB > 35% would be individually excluded for statistical analysis. Downfield spectra were fitted with a basis set consisting of nine Gaussian peaks ranging in frequency from 6.83 to 8.49 ppm, and the baseline stiffness was set using the control parameter "DKNTMN" = 5, following a previous study[24, 65]. A composite peak (8.x ppm) was also fitted to represent the region of 8.18-8.37 ppm[65]. Due to the relatively low SNR of downfield signals compared to upfield signals, the fitting results of downfield signals with CRLB > 50% would be individually excluded for statistical analysis. Therefore, the sample size for each metabolite was varied. The sample size and CRLB for each MRS resonance in each group were listed in Supplementary Table 8. For each metabolite, the SNR was calculated individually by dividing the fitted signal amplitude by the standard deviation of the spectral noise. Specifically, metabolite signal amplitudes were obtained by fitting each respective resonance peak using LCModel. In addition, the spectral noise was estimated as the standard deviation of the last 200 points of the free induction decay (FID), acquired from a signal-free region. To enable comparison across subjects and groups, the SNR was further normalized by the voxel size, the results were presented in "institutional units" (i.u.). The robustness of the primary normalization method was assessed by performing an alternative normalization using total creatine (tCr) as an internal reference metabolite. Specifically, ratios (e.g., NAA/tCr, DF6.8/tCr) were derived by dividing the peak area of the target metabolite by the peak area of tCr.

The tumor size was measured using the anatomical T_2W images. The TGR in the TB group was fitted using nonlinear least-squares regression in MATLAB 2018b. The exponential model fitted all tumor growth curves with high accuracy, as evidenced by R^2 values (mean ± SD = 0.980 ± 0.027). To perform the correlation analysis, the average downfield signals from late-stage timepoints for each TB rat were calculated and correlated with the corresponding TGR.

Statistics and Reproducibility

Sample sizes were determined according to previous literature[12, 24] and our preliminary experiments. For analysis of inter-group differences in the normalized MRS spectra, outliers were first removed based on the mean ± 1.75 × interquartile range (IQR). Then, a mixed-effects model was applied to account for repeated measures and sample dependence within groups, with samples as a random effect and group as a fixed effect. In untargeted metabolomics statistics between HC and TB tissues, normal data were compared using independent t-tests, while non-normal data were compared with Wilcoxon rank-sum tests. For all correlation analyses, Pearson correlation was used for normal distributions, and Spearman's rank correlation was used for non-normal distributions. Statistical significance was set at + $P < 0.1$, * $P < 0.05$, ** $P < 0.01$, *** $P < 0.001$. The Benjamini & Hochberg false discovery rate adjusted p-FDR was also calculated. All statistical analyses were performed using Python version 3.10.10. Blinding and randomization were not performed.

Data Availability

The main data supporting the results of this study are available within the paper and the supplementary information. The raw and analysed data are available from the corresponding author upon reasonable request, and we will respond within two weeks. Source data underlying graphs can be obtained from Supplementary data.

Code Availability

The sequence development is based on the 7T Bruker BioSpin platform, with the system version ParaVision 360V3.0. The MC-PRESS sequence was developed using the PRESS sequence provided by the platform. Postprocessing code will be shared upon request, and we will respond within two weeks.

Acknowledgements

This work was supported in part by the National Natural Science Foundation of China (Grant No. 32301159, and 82572290) and Zhejiang Provincial Natural Science Foundation of China (Z25H180012) and the National Key Research and Development Program of China (2021YFA1101700).

Author Contributions

MRS data acquisition: X.Z, C.Y, K.Z, M.W. Sequence development: X.Z, M.W. Data post-processing: X.Z, M.W. Tissue sampling: X.Z, C.Y, S.C, YB.L, M.W. Statistical: X.Z, M.W. Funding acquisition: M.W. Writing-original draft: X.Z. Writing—review & editing: X.Z, J.Z, YC.L, M.W. All authors read the final version of the manuscript and provided critical feedback.

Ethics declarations

Competing interests

The authors declare no competing interests.

References

1. Roca A, *et al.* Effect of Intrapartum Azithromycin vs Placebo on Neonatal Sepsis and Death. *Jama* **329**, (2023).
2. Schaff LR, Mellinghoff IK. Glioblastoma and Other Primary Brain Malignancies in Adults. *Jama* **329**, (2023).
3. Louis DN, *et al.* The 2021 WHO Classification of Tumors of the Central Nervous System: a summary. *Neuro Oncol* **23**, 1231-1251 (2021).
4. Kurokawa R, *et al.* Major Changes in 2021 World Health Organization Classification of Central Nervous System Tumors. *RadioGraphics* **42**, 1474-1493 (2022).
5. Mori S, Eleff SM, Pilatus U, Mori N, van Zijl PCM. Proton NMR spectroscopy of solvent-saturable resonances: A new approach to study pH effects in Situ. *Magnetic Resonance in Medicine* **40**, 36-42 (2005).
6. Fichtner ND, Henning A, Zoelch N, Boesch C, Kreis R. Elucidation of the downfield spectrum of human brain at 7 T using multiple inversion recovery delays and echo times. *Magnetic Resonance in Medicine* **78**, 11-19 (2016).
7. Borbath T, Murali-Manohar S, Wright AM, Henning A. In vivo characterization of downfield peaks at 9.4 T: T2 relaxation times, quantification, pH estimation, and assignments. *Magnetic Resonance in Medicine* **85**, 587-600 (2020).
8. Li Y, *et al.* Leveraging adenosine triphosphate for cancer theranostics. *Theranostics* **15**, 4708-4733 (2025).
9. Kreis R, Zwygart K, Boesch C, Nuoffer JM. Reproducibility of cerebral phenylalanine levels in patients with phenylketonuria determined by 1H-MR spectroscopy. *Magnetic Resonance in Medicine* **62**, 11-16 (2009).
10. Dziadosz M, Bogner W, Kreis R. Non-water-excitation MR spectroscopy techniques to explore exchanging protons in human brain at 3 T. *Magnetic Resonance in Medicine* **84**, 2352-2363 (2020).
11. In vivo characterization of the downfield part of 1H MR spectra of human brain at 9.4T: Magnetization exchange with water and relation to conventionally determined metabolite content. (2017).
12. Gonçalves SI, Simões RV, Shemesh N. Short TE downfield magnetic resonance spectroscopy in a mouse model of brain glioma. *Magnetic Resonance in Medicine* **88**, 524-536 (2022).
13. Povazan M, Schar M, Gillen J, Barker PB. Magnetic resonance spectroscopic imaging of downfield proton resonances in the human brain at 3 T. *Magn Reson Med*, (2022).
14. Özdemir İ, *et al.* Downfield Proton MRSI with whole-brain coverage at 3T. (2023).
15. Gonçalves SI, Ligneul C, Shemesh N. Short echo time relaxation-enhanced MR spectroscopy reveals broad downfield resonances. *Magnetic Resonance in Medicine* **82**, 1266-1277 (2019).
16. Zöllner HJ, *et al.* Comparison of different linear-combination modeling algorithms for short-TE proton spectra. *NMR in Biomedicine* **34**, (2021).
17. Feng S, Liu Y. Metabolomics of Glioma. In: *Cancer Metabolomics*) (2021).
18. Mukherjee AG, *et al.* Recent advances in understanding brain cancer metabolomics: a review. *Med Oncol* **40**, 220 (2023).
19. Gaca-Tabaszewska M, Bogusiewicz J, Bojko B. Metabolomic and Lipidomic Profiling of Gliomas—A New Direction in Personalized Therapies. *Cancers* **14**, (2022).

20. Miller JJ, *et al.* Isocitrate dehydrogenase (IDH) mutant gliomas: A Society for Neuro-Oncology (SNO) consensus review on diagnosis, management, and future directions. *Neuro-Oncology* **25**, 4-25 (2023).
21. Xiao X, *et al.* Tumor size as a significant prognostic factor in T1 gastric cancer: a Surveillance, Epidemiology, and End Results (SEER) database analysis. *BMC Gastroenterol* **23**, 121 (2023).
22. Kazda T, *et al.* Advanced MRI increases the diagnostic accuracy of recurrent glioblastoma: Single institution thresholds and validation of MR spectroscopy and diffusion weighted MR imaging. *NeuroImage: Clinical* **11**, 316-321 (2016).
23. MacMillan EL, *et al.* Magnetization exchange with water andT1relaxation of the downfield resonances in human brain spectra at 3.0 T. *Magnetic Resonance in Medicine* **65**, 1239-1246 (2011).
24. Özdemir I, *et al.* Downfield Proton MRSI at 3 Tesla: A Pilot Study in Human Brain Tumors. *Cancers* **15**, (2023).
25. Prisciandaro JJ, Zollner HJ, Murali-Manohar S, Oeltzschner G, Edden RAE. More than one-half of the variance in in vivo proton MR spectroscopy metabolite estimates is common to all metabolites. *NMR Biomed* **36**, e4907 (2023).
26. Vejdani Afkham B, Alonso-Ortiz E. On the impact of B0 shimming algorithms on single-voxel MR spectroscopy. *Magn Reson Med* **93**, 42-50 (2025).
27. Snaebjornsson MT, Janaki-Raman S, Schulze A. Greasing the Wheels of the Cancer Machine: The Role of Lipid Metabolism in Cancer. *Cell Metabolism* **31**, 62-76 (2020).
28. Broadfield LA, Pane AA, Talebi A, Swinnen JV, Fendt SM. Lipid metabolism in cancer: New perspectives and emerging mechanisms. *Dev Cell* **56**, 1363-1393 (2021).
29. Traut TW. Physiological concentrations of purines and pyrimidines. *Mol Cell Biochem* **140**, 1-22 (1994).
30. Mullen NJ, Singh PK. Nucleotide metabolism: a pan-cancer metabolic dependency. *Nature Reviews Cancer* **23**, 275-294 (2023).
31. Wishart DS. Metabolomics for Investigating Physiological and Pathophysiological Processes. *Physiol Rev* **99**, 1819-1875 (2019).
32. Graaf RAd. *In Vivo NMR Spectroscopy: Principles and Techniques*. Wiley (2018).
33. Behar KL, Rothman DL, Spencer DD, Petroff OAC. Analysis of macromolecule resonances in 1H NMR spectra of human brain. *Magnetic Resonance in Medicine* **32**, 294-302 (2005).
34. Howe FA, *et al.* Metabolic profiles of human brain tumors using quantitative in vivo 1H magnetic resonance spectroscopy. *Magnetic Resonance in Medicine* **49**, 223-232 (2003).
35. Dienel GA. Metabolomic Assays of Postmortem Brain Extracts: Pitfalls in Extrapolation of Concentrations of Glucose and Amino Acids to Metabolic Dysregulation In Vivo in Neurological Diseases. *Neurochemical Research* **44**, 2239-2260 (2018).
36. A Henning AF, C Boesch, P Boesiger, R Kreis. Downfield Spectra at Ultrahigh Field. *Proc Intl Soc Mag Reson Med 16*, (2008).
37. Giuliani P, *et al.* Evidence for purine nucleoside phosphorylase (PNP) release from rat C6 glioma cells. *Journal of Neurochemistry* **141**, 208-221 (2017).
38. Lee DC, *et al.* Amino Acid and Glucose Fermentation Maintain ATP Content in Mouse and Human Malignant Glioma Cells. *ASN Neuro* **16**, (2024).
39. Wu CY-J, *et al.* Tumor-Associated Microglia Secrete Extracellular ATP to Support Glioblastoma Progression. *Cancer Research* **84**, 4017-4030 (2024).

40. Hoefemann M, Döring A, Fichtner ND, Kreis R. Combining chemical exchange saturation transfer and1H magnetic resonance spectroscopy for simultaneous determination of metabolite concentrations and effects of magnetization exchange. *Magnetic Resonance in Medicine* **85**, 1766-1782 (2020).
41. Fichtner ND, *et al.* In vivo characterization of the downfield part of 1H MR spectra of human brain at 9.4 T: Magnetization exchange with water and relation to conventionally determined metabolite content. *Magnetic Resonance in Medicine* **79**, 2863-2873 (2017).
42. Özdemir İ, Etyemez S, Barker PB. Amide mapping in the human brain using downfield MRSI at 3 T and 7 T. *Magnetic Resonance in Medicine*, (2025).
43. Schanda P, Van Melckebeke H, Brutscher B. Speeding Up Three-Dimensional Protein NMR Experiments to a Few Minutes. *Journal of the American Chemical Society* **128**, 9042-9043 (2006).
44. Shemesh N, Dumez JN, Frydman L. Longitudinal Relaxation Enhancement in 1H NMR Spectroscopy of Tissue Metabolites via Spectrally Selective Excitation. *Chemistry – A European Journal* **19**, 13002-13008 (2013).
45. Schanda P. Fast-pulsing longitudinal relaxation optimized techniques: Enriching the toolbox of fast biomolecular NMR spectroscopy. *Progress in Nuclear Magnetic Resonance Spectroscopy* **55**, 238-265 (2009).
46. Zhou J, Payen J-F, Wilson DA, Traystman RJ, van Zijl PCM. Using the amide proton signals of intracellular proteins and peptides to detect pH effects in MRI. *Nature Medicine* **9**, 1085-1090 (2003).
47. Souza TKF, *et al.* Image and motor behavior for monitoring tumor growth in C6 glioma model. *PLoS One* **13**, e0201453 (2018).
48. Silva ACd, *et al.* Tumor growth analysis by magnetic resonance imaging of the C6 glioblastoma model with prospects for the assessment of magnetohyperthermia therapy. *Einstein (São Paulo)* **10**, 11-15 (2012).
49. Case KC, Schmidtke MW, Greenberg ML. The paradoxical role of inositol in cancer: a consequence of the metabolic state of a tumor. *Cancer and Metastasis Reviews* **41**, 249-254 (2022).
50. Trock BJ. Application of metabolomics to prostate cancer. *Urologic Oncology: Seminars and Original Investigations* **29**, 572-581 (2011).
51. Jordan KW, Cheng LL. NMR-based metabolomics approach to target biomarkers for human prostate cancer. *Expert Review of Proteomics* **4**, 389-400 (2014).
52. Knörnschild F, *et al.* Correlations of blood and brain NMR metabolomics with Alzheimer's disease mouse models. *Translational Psychiatry* **15**, (2025).
53. Li Y. T1 and T2 Metabolite Relaxation Times in Normal Brain at 3T and 7T. *Journal of Molecular Imaging & Dynamics* **02**, (2013).
54. Nanga RPR, *et al.* Identification of l-Tryptophan by down-field 1H MRS: A precursor for brain NAD+ and serotonin syntheses. *Magnetic Resonance in Medicine* **88**, 2371-2377 (2022).
55. Wang J, *et al.* Serum metabolomics for early diagnosis of esophageal squamous cell carcinoma by UHPLC-QTOF/MS. *Metabolomics* **12**, (2016).
56. Zhou Z, *et al.* Metabolite annotation from knowns to unknowns through knowledge-guided multi-layer metabolic networking. *Nat Commun* **13**, 6656 (2022).
57. Sumner LW, *et al.* Proposed minimum reporting standards for chemical analysis. *Metabolomics* **3**, 211-221 (2007).

58. Wishart DS, *et al.* HMDB: the Human Metabolome Database. *Nucleic Acids Research* **35**, D521-D526 (2007).
59. Wiklund S, *et al.* Visualization of GC/TOF-MS-based metabolomics data for identification of biochemically interesting compounds using OPLS class models. *Anal Chem* **80**, 115-122 (2008).
60. Trygg J, Wold S. Orthogonal projections to latent structures (O-PLS). *Journal of Chemometrics* **16**, 119-128 (2002).
61. Dreher W, Leibfritz D. New method for the simultaneous detection of metabolites and water in localized in vivo 1H nuclear magnetic resonance spectroscopy. *Magn Reson Med* **54**, 190-195 (2005).
62. Provencher SW. Automatic quantitation of localized in vivo 1H spectra with LCModel. *NMR Biomed* **14**, 260-264 (2001).
63. Soher BJ, *et al.* Vespa: Integrated applications for RF pulse design, spectral simulation and MRS data analysis. *Magnetic Resonance in Medicine* **90**, 823-838 (2023).
64. Waxmann P, *et al.* A new sequence for shaped voxel spectroscopy in the human brain using 2D spatially selective excitation and parallel transmission. *NMR in Biomedicine* **29**, 1028-1037 (2016).
65. Özdemir İ, Etyemez S, Barker PB. High-field downfield MR spectroscopic imaging in the human brain. *Magnetic Resonance in Medicine*, (2024).

Tables

Table 1 Correlation analysis of specific omics metabolite with corresponding MRS signals.

Metabolite compound	CAS number	Resonance(ppm)	TE = 6.9 ms				TE = 15 ms			
			n	r	*P*	p-FDR	n	r	*P*	p-FDR
Glutamate	56-86-0	2.04/2.35/3.75	9	**0.800**	**0.010**	0.063	9	**0.786**	**0.012**	0.154
Aspartate (NAA)	56-84-8	2.01/2.49/2.67/4.38	9	**0.933**	**<0.001**	0.001	9	**0.909**	**0.001**	0.055
		7.82	9	-0.439	0.237	0.447	9	0.114	0.770	0.919
Glutamine	56-85-9	2.12/2.46/3.77	5	0.402	0.502	0.719	8	**0.814**	**0.014**	0.154
		6.8	9	-0.800	0.010	0.063	9	-0.550	0.125	0.362
		7.5	9	-0.633	0.067	0.195	9	-0.467	0.205	0.470
Creatine (tCr)	57-00-1	3.03/3.93	9	0.548	0.127	0.279	9	0.615	0.078	0.297
Choline (tCh)	62-49-7	3.21/3.66/4.31	9	-0.239	0.536	0.737	9	-0.209	0.589	0.790
Lactate	50-21-5	1.31/4.10	9	-0.402	0.284	0.488	8	-0.467	0.244	0.537
Taurine	107-35-7	3.25/3.42	9	0.433	0.244	0.447	9	0.317	0.406	0.657
myo-Inositol	87-89-8	3.27/3.52/3.61/4.05	9	-0.607	0.083	0.217	9	-0.387	0.304	0.539
Glutathione disulfide (GSH)	27025-41-8	2.15/2.55/2.93/2.98/3.77/4.56	7	-0.328	0.472	0.702	6	-0.386	0.450	0.678
		7.154	9	0.522	0.149	0.315	9	**0.671**	**0.048**	0.245
		8.177	8	0.403	0.323	0.537	8	-0.520	0.187	0.462
4-Aminobutyric acid (GABA)	56-12-2	1.89/2.28/3.00	9	-0.217	0.576	0.754	9	0.583	0.099	0.303
Phenylalanine	63-91-2	7.30	9	-0.031	0.936	0.977	9	0.348	0.358	0.615
		7.45	9	-0.097	0.804	0.884	9	0.117	0.764	0.919
Histidine	71-00-1	7.1	9	-0.855	0.003	0.055	9	-0.684	0.042	0.245
		7.8	9	-0.779	0.013	0.063	9	0.067	0.864	0.950
Tryptophan	73-22-3	7.31/7.20/7.28	9	0.158	0.685	0.819	9	0.513	0.157	0.432
Tyrosine	60-18-4	6.89	9	-0.011	0.977	0.977	9	0.480	0.191	0.462
		7.19	9	-0.162	0.677	0.819	9	0.417	0.264	0.539
Adenosine 5'-diphosphate (ADP)	58-64-0	6.755	9	-0.473	0.199	0.391	9	0.028	0.944	0.998
		~8.2	8	-0.631	0.093	0.232	8	-0.006	0.990	1.000
		8.51	9	-0.254	0.510	0.719	8	-0.234	0.577	0.790
Adenosine monophosphate (AMP)	61-19-8	6.755	9	-0.778	0.014	0.063	9	-0.669	0.049	0.245
		~8.2	8	-0.758	0.029	0.106	8	0.227	0.588	0.790
		8.51	9	0.102	0.795	0.884	8	-0.683	0.062	0.267
Adenosine	58-61-7	6.755	9	0.135	0.730	0.854	9	0.083	0.831	0.933
		~8.2	8	-0.217	0.606	0.758	8	-0.514	0.193	0.462
		8.51	9	-0.012	0.976	0.977	8	-0.322	0.436	0.678
Inosine	58-63-9	6.755	9	-0.817	0.007	0.063	9	-0.392	0.296	0.539
		~8.2	8	-0.828	0.011	0.063	8	0.114	0.788	0.919
		8.51	9	0.019	0.961	0.977	8	-0.776	0.023	0.193
Hypoxanthine	68-94-0	6.755	9	-0.316	0.407	0.640	9	-0.406	0.278	0.539
		~8.2	8	-0.790	0.020	0.079	8	-0.007	0.987	1.000
		8.51	9	-0.552	0.123	0.279	8	-0.651	0.081	0.297
Xanthine	69-89-6	6.755	9	**0.687**	**0.041**	0.141	9	0.102	0.794	0.919
		~8.2	8	0.449	0.265	0.470	8	0.139	0.743	0.919
		8.51	9	-0.224	0.563	0.754	8	0.626	0.097	0.303
Uric acid	69-93-2	6.755	9	**0.801**	**0.010**	0.063	9	0.335	0.379	0.632
		~8.2	8	0.693	0.057	0.184	8	0.041	0.924	0.996
		8.51	9	-0.299	0.435	0.665	8	0.681	0.063	0.267
Deoxyadenosine	958-09-8	6.755	9	**0.783**	**0.013**	0.063	9	0.583	0.099	0.303
		~8.2	8	**0.810**	**0.015**	0.063	8	0.000	1.000	1.000
		8.51	9	0.367	0.332	0.537	8	**0.762**	**0.028**	0.193
Deoxyinosine	890-38-0	6.755	9	**0.933**	**<0.001**	0.001	9	**0.833**	**0.005**	0.138
		~8.2	8	0.667	0.071	0.195	8	-0.262	0.531	0.769
		8.51	9	-0.100	0.798	0.884	8	**0.752**	**0.028**	0.193
Ribose-1-phosphate	14075-00-4	6.755	8	0.658	0.071	0.195	8	-0.429	0.289	0.539
		~8.2	9	0.500	0.170	0.346	8	0.310	0.456	0.678
		8.51	9	-0.067	0.865	0.933	9	0.100	0.798	0.919
Deoxyribose-1-phosphate	17210-42-3	6.755	8	-0.624	0.098	0.234	8	0.107	0.802	0.919
		~8.2	9	-0.200	0.606	0.758	8	-0.849	0.008	0.147
		8.51	9	-0.850	0.004	0.055	9	-0.408	0.275	0.539

NOTE: "**Metabolite compound**" denoted metabolites identified via metabolomics. For the upfield region, the correlations between MRS signals and their corresponding omics-identified metabolites are presented, as their metabolic origins are relatively well-established. Given that NAA is unstable ex vivo and hydrolyzes into aspartate and acetate, aspartate is selected as a surrogate marker for NAA. PCr is also unstable and has been reported to be rapidly consumed in ex vivo glioblastoma samples, therefore only the correlation between creatine and tCr signals is shown. In addition, GSH is prone to oxidation in the extracellular environment, and its oxidized form is glutathione disulfide (GSSG), thus GSSG is used as an in vitro representation of GSH. For the downfield signals, potential contributors reported in prior literature were included, such as NAA (amide proton), glutathione (amide proton), ATP (adenosine and amino group), phenylalanine (phenyl moiety), histidine (imidazole moiety), Gln (amide proton), tryptophan (indole moiety) and tyrosine (phenol moiety). Due to the instability of ATP under ex vivo conditions, downstream metabolites in its metabolic pathway (Supplementary Figure 5) are selected as surrogate indicators for its ex vivo characterization. "**CAS number**" (Chemical Abstracts Service Registry Number) serves as a unique numerical identifier for every chemical substance appearing in scientific literature, and is assigned by the American Chemical Abstracts Service. The chemical shift for the "**Resonance**" of all the metabolites are obtained from reference[28]. For upfield metabolites, correlation analysis was performed between the metabolite levels detected by untargeted metabolomics and the normalized values derived from fitted upfield MRS signals. For downfield metabolites, correlation analysis was performed between the metabolite levels detected by untargeted metabolomics and the normalized values derived from fitted downfield MRS signals with the closest resonance frequencies. For example, downfield metabolite ATP, which resonates at 6.755 ppm, ~8.2 ppm, and 8.51 ppm, was correlated with DF6.83, DF8.18, and DF8.49, respectively. "**n**" represents the actual number included in the correlation analysis. Values with a correlation coefficient $r > 0.5$ and $P < 0.1$ are marked in blue, while values with a correlation coefficient $r > 0.5$ and $P < 0.05$ are marked in blue and **bolded**.

Figure captions

Figure 1. MC-PRESS and visualization of spectra of the HC and ES/LS gliomas at two TEs. (a) MC-PRESS sequence schedule. Outer volume suppression (OVS) pre-saturation pulses and an inversion pulse were applied sequentially prior to PRESS localization excitation. **(b)** Representative downfield (6~10 ppm) and upfield (0~4 ppm) magnetic resonance spectroscopy (MRS) spectra of health control rats (HC) and early-stage/late-stage (ES/LS) gliomas at two echo times (TE). The rat brain structural image is shown, with the red square representing the MRS voxel. The blue line indicates TE = 15 ms, while the black line indicates TE = 6.9 ms. The vertical scale for the upfield signals is consistent across all samples, while the downfield signals are displayed with a vertical scale expanded by a factor of 6 compared to the upfield signals. DF8.x refers to the sum of DF8.18, DF8.24, and DF8.37. **(c)** Average normalized spectra in the HC and ES/LS gliomas groups (HC: n = 10, ES: n = 8, LS: n = 12). Solid lines represent the mean spectra, and shaded regions indicate the 95% confidence interval of the mean.

Figure 2. Altered MRS signals in HC and ES/LS glioma groups. (a) Mixed-effects model comparison for upfield signals of three groups at two TEs. Red boxes indicate echo time (TE) = 6.9 ms, while blue boxes represent TE = 15 ms. Box plots overlaid with scatter points display individual data distributions. The boxes represent the interquartile range (IQR), the central line indicates the median, whiskers extend to data points within 1.5 × IQR, and points beyond are considered outliers. Points from the same sample at different TEs are connected by gray lines. GSH: glutathione, Ins: inositol, Lac: lactate, NAA: N-acetyl aspartate, Tau: taurine, tCh: total choline, tCr: total creatine, Glu: glutamate, Gln: glutamine, GABA: γ-aminobutyric acid. **(b)** Mixed-effects model comparison for downfield signals of three groups at two TEs. **(c)** Mixed-effects model comparison for the downfield sum peak signal of three groups at TE = 6.9 ms. **(d)** Mixed-effects model comparison for the downfield sum peak signal of three groups at TE = 15 ms. **(e)** Mixed-effects model comparison for water signals of three groups at TE = 6.9 ms. **(f)** Mixed-effects model

comparison for water signals of three groups at TE = 15 ms. The sample sizes used for statistical analysis are provided in Supplementary Table 8. * $P < 0.05$, ** $P < 0.01$, *** $P < 0.001$.

Figure 3. Untargeted metabolomic profiling of normal and tumor rat brain tissues. (a) Heatmap of metabolomics metabolite clustering for health control (HC) tissue samples (n = 4) and tumor-bearing (TB) tissue samples (n = 5). Colors represent relative metabolite abundance, with red indicating higher abundance and blue indicating lower abundance. **(b)** Distribution of metabolite categories identified by untargeted metabolomics. **(c)** Unsupervised principal component analysis (PCA) score plot of untargeted metabolomics data, with all sample points falling within the 95% confidence interval. **(d)** Supervised orthogonal projections to latent structures-discriminant analysis (OPLS-DA) score plot of untargeted metabolomics data, showing distinct differences between groups, with all sample points falling within the 95% confidence interval. **(e)** Permutation plot tests of OPLS-DA model. All Q2 points from left to right are lower than the original blue Q2 points on the right side, indicating that the model is robust and reliable without overfitting. **(f)** Volcano plot selecting differential metabolites based on variable importance in the projection (VIP) (VIP > 1) and *P* ($P < 0.05$). The x-axis shows fold change (log2) and the y-axis shows *P* (negative log10) from the t-test. The fold change is defined as the ratio of quantitative values between two groups (TB/HC). Red points indicate significantly upregulated metabolites, blue points indicate significantly downregulated metabolites, and gray points indicate metabolites without significant differences. **(g)** Hierarchical clustering heatmap of the top 10 significantly upregulated and downregulated metabolites identified. The x-axis represents the samples, the y-axis represents the differential metabolites, and the color blocks at different positions indicate the z-scores of the corresponding metabolites.

Figure 4. Metabolite category–based principal component patterns in normal and tumor tissues. (a) Explained variance plot of principal components derived from metabolite category–level untargeted metabolomics data. The line plot shows the explained variance for each principal component, while the bar chart represents the cumulative explained variance. Principal components are selected based on a threshold

of no more than 90% of the total explained variance. **(b)** Mean principal component scores of health control (HC) and tumor (TB) tissues (HC: n = 4, TB: n = 5) for each principal component. The most significant intergroup differences ($P \leq 0.001$) involved nucleotides, benzenoids, and lipids. Significant differences were analyzed using a two-sample independent t-test: * $P < 0.05$, ** $P < 0.01$, *** $P < 0.001$.

Figure 5. Correlation patterns between MRS signals and individual metabolites in untargeted metabolomics. (a) Heatmaps of correlation coefficients and correlation significance between upfield signals and untargeted omics metabolites at two TEs. The vertical axis represents 1425 omics metabolites (8 metabolite classes), as shown in the table on the left, and the horizontal axis corresponds to the ten upfield signals. In the correlation significance matrix, red represents metabolites with $r \geq 0.7$ and p-FDR < 0.10, while blue represents metabolites with $r \leq -0.7$ and p-FDR < 0.10. **(b)** Heatmaps of correlation coefficients and correlation significance between downfield signals and untargeted omics metabolites at two echo times (TE). The vertical axis represents the omics metabolites, while the horizontal axis corresponds to the 10 downfield signals. **(c)** Difference correlation coefficients matrix between two TEs for upfield and downfield signals. It was calculated by subtracting the correlation matrix at TE = 15 ms from the correlation matrix at TE = 6.9 ms.

Figure 6. Correlation of upfield and downfield MRS signals with metabolite categories. (a) Heatmap of the correlation between the composite principal component analysis (PCA) score vector of each metabolite category and upfield signals at two echo times (TE) (n = 9). **(b)** Heatmap of the correlation between the composite PCA score vector of each metabolite category and downfield signals at two TEs (n = 9). A number of downfield signals showed correlations with nucleotides and benzenoids at TE = 6.9 ms. **(c)** Bar chart of the statistical probability for strong correlations ($r > 0.7$) between each metabolomic category and downfield signals at two TEs. DF6.83, DF8.18, and DF8.x exhibited the highest probability distribution of strong correlation with nucleotides at TE = 6.9 ms (probability density > 0.24, as indicated by the red dashed line). * $P < 0.05$, ** $P < 0.01$, *** $P < 0.001$.

Figure 7. Correlation between MRS signals and tumor growth parameters. (a) Schematic representation of tumor progression. The red segmentation mask delineates the tumor region. **(b)** Fitting of the exponential growth curve of brain tumors in tumor-bearing rats (n = 7). The black dashed line (tumor size = 50 μL) represents the boundary between early-stage and late-stage groups. **(c)** Significant correlations between tumor size and upfield signals at two echo times (TE). **(d)** Significant correlations between tumor size and downfield signals. Only DF8.18 and DF8.24 showed correlations with tumor size at echo time = 6.9 ms. **(e)** Significant correlations between tumor growth rate (TGR) and MRS signals at two TEs. Ins and TGR show good linear consistency at TE = 15 ms. Shaded areas represent the 95% confidence interval of the fitted linear regression. The sample sizes used for correlation analysis are shown in Supplementary Table 4.

Editor Summary:
Integrated magnetic resonance spectroscopy and untargeted metabolomics help elucidate the metabolic origins of downfield MRS signals in glioma, enabling non invasive capturing adenosine triphosphate (ATP)-associated nucleotide metabolism.

Peer Review Information:

Communications Biology thanks the anonymous reviewers for their contribution to the peer review of this work. Primary Handling Editors: Zheng-Jiang Zhu and Joao Valente. A peer review file is available.

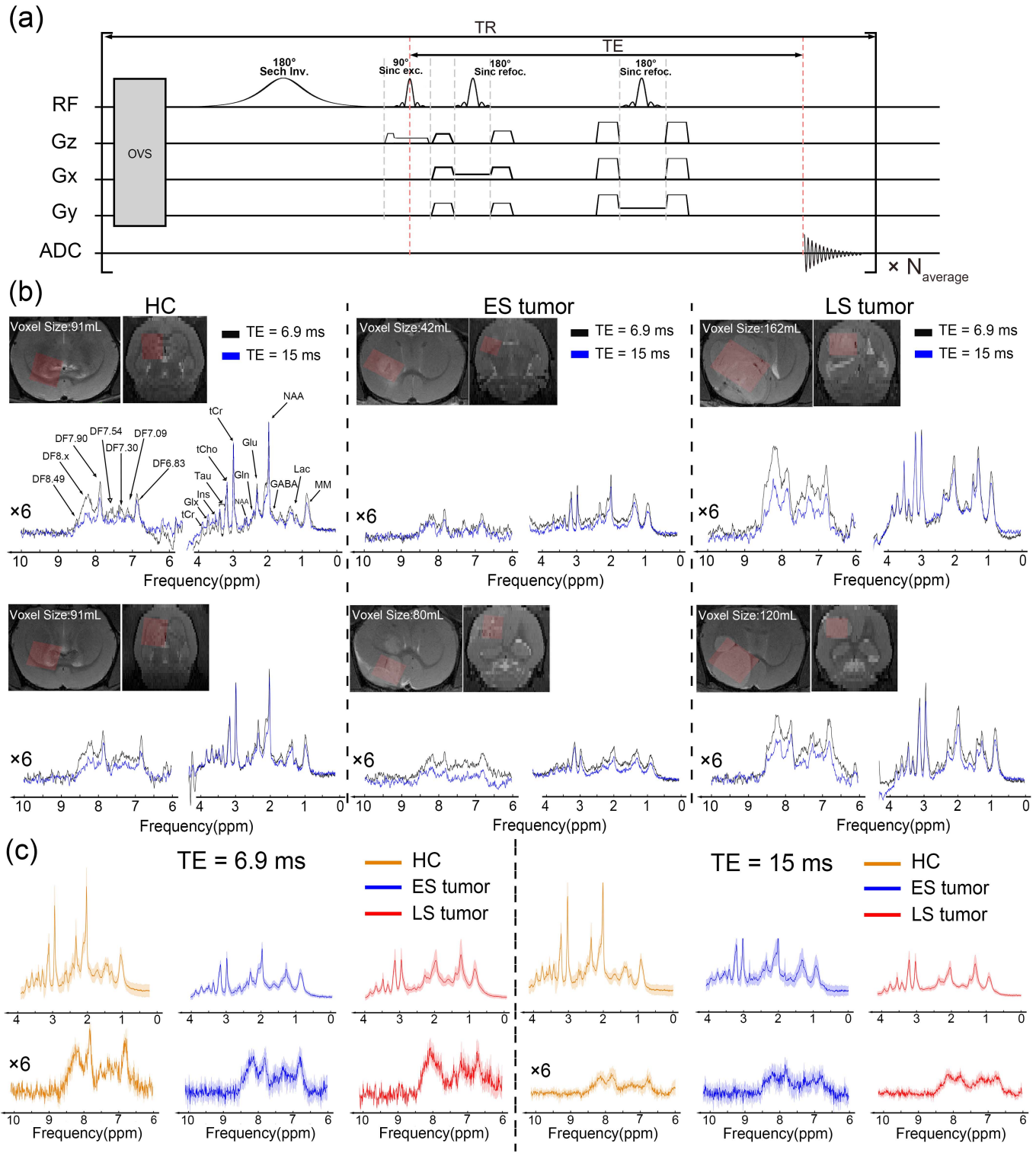
(a)
TR
TE
180° Sech Inv.
90° Sinc exc.
180° Sinc refoc.
180° Sinc refoc.
RF
Gz
Gx
Gy
ADC
OVS
× N average
(b)
HC
ES tumor
LS tumor
Voxel Size:91mL
Voxel Size:42mL
Voxel Size:162mL
Voxel Size:91mL
Voxel Size:80mL
Voxel Size:120mL
TE = 6.9 ms
TE = 15 ms
DF8.49
DF8.x
DF7.90
DF7.54
DF7.30
DF7.09
DF6.83
tCr
tCho
Tau
Ins
Glx
tCr
NAA
Glu
Gln
NAA
GABA
Lac
MM
×6
Frequency(ppm)
(c)
TE = 6.9 ms
TE = 15 ms
HC
ES tumor
LS tumor
×6
Frequency(ppm)

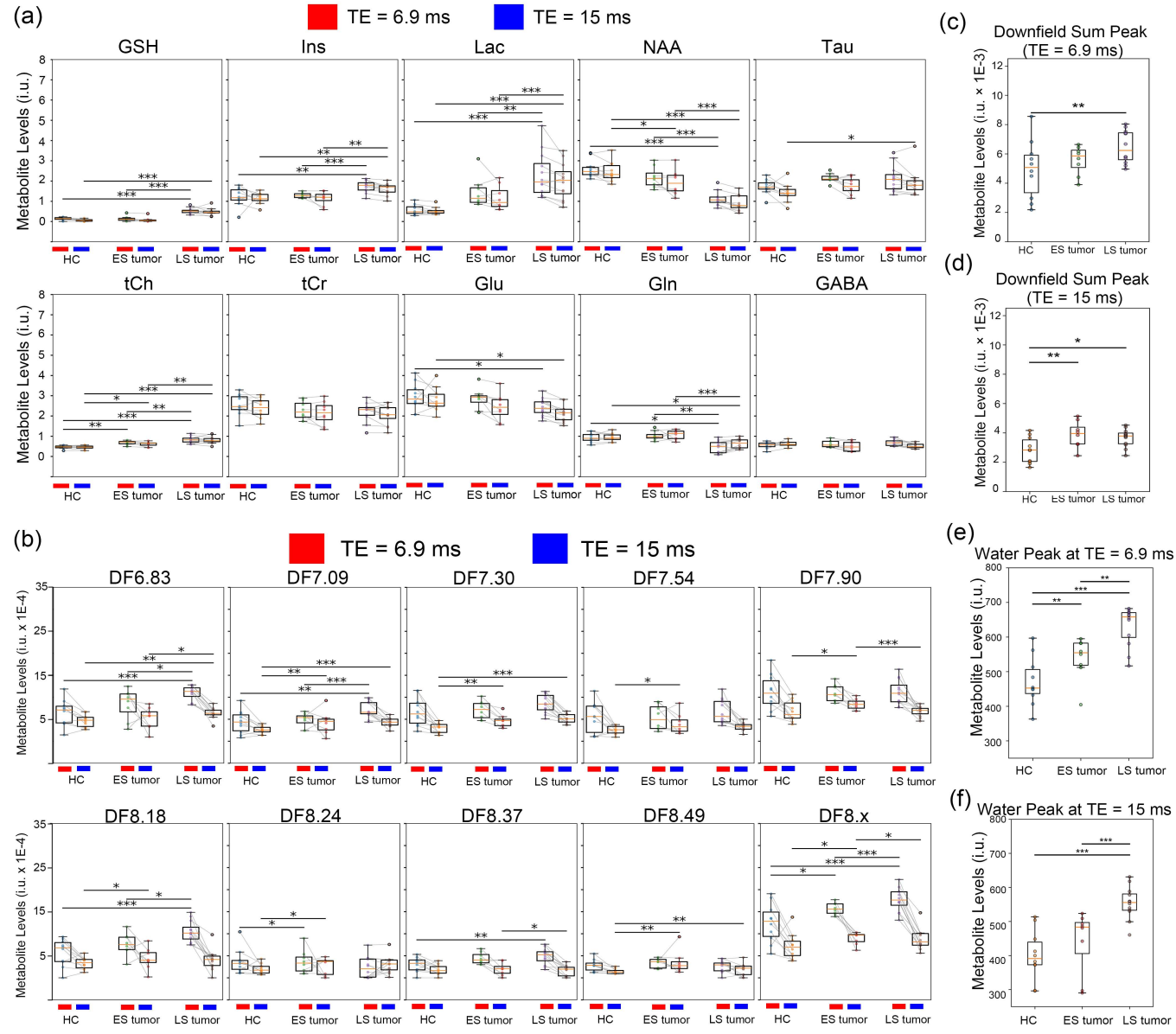
(a)
TE = 6.9 ms
TE = 15 ms
GSH
Ins
Lac
NAA
Tau
tCh
tCr
Glu
Gln
GABA
Metabolite Levels (i.u.)
HC
ES tumor
LS tumor
(b)
DF6.83
DF7.09
DF7.30
DF7.54
DF7.90
DF8.18
DF8.24
DF8.37
DF8.49
DF8.x
Metabolite Levels (i.u. x 1E-4)
(c)
Downfield Sum Peak
(TE = 6.9 ms)
Metabolite Levels (i.u. × 1E-3)
(d)
Downfield Sum Peak
(TE = 15 ms)
(e)
Water Peak at TE = 6.9 ms
Metabolite Levels (i.u.)
(f)
Water Peak at TE = 15 ms

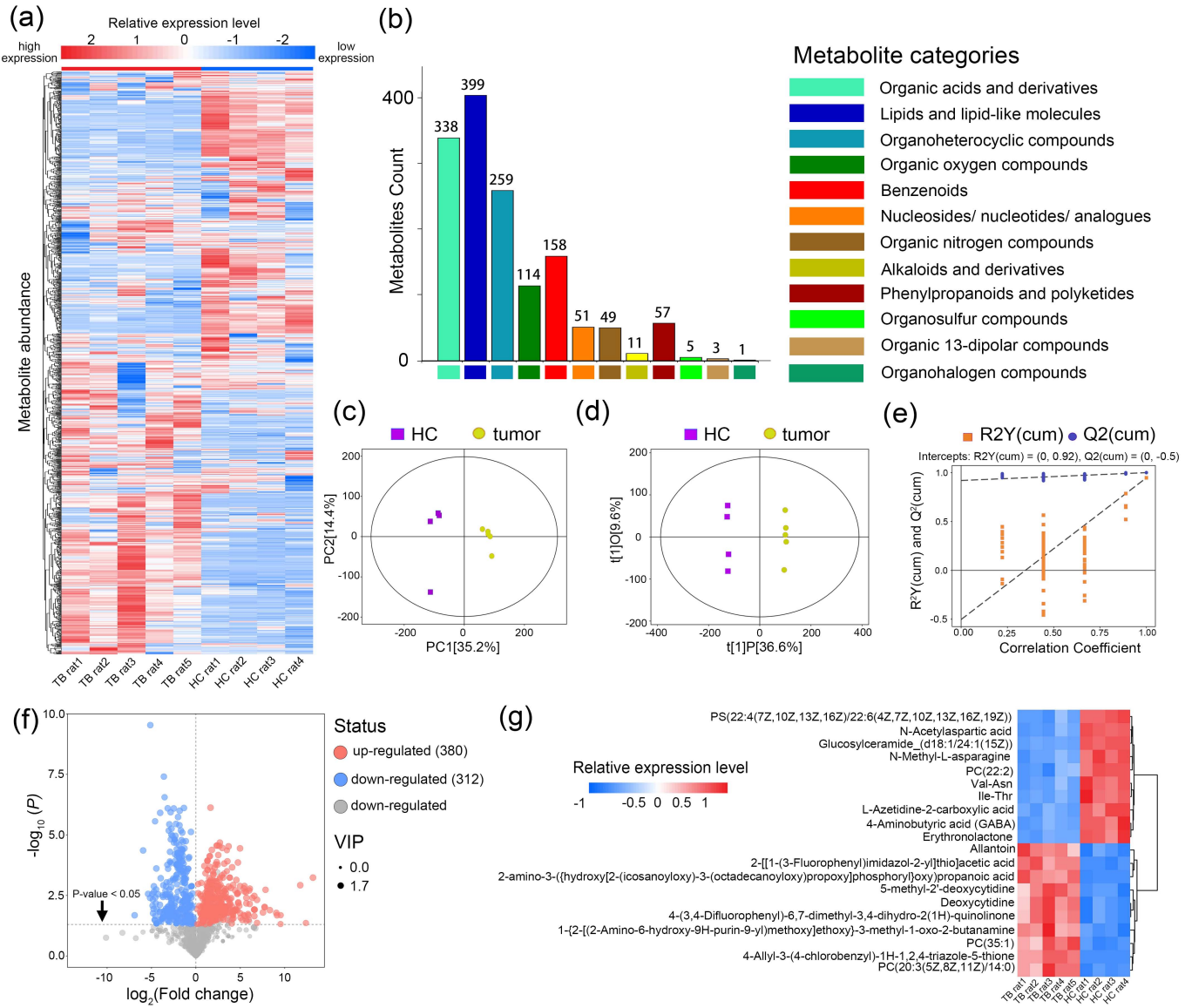
(a)
Relative expression level
high expression
low expression
2 1 0 -1 -2
Metabolite abundance
TB rat1
TB rat2
TB rat3
TB rat4
TB rat5
HC rat1
HC rat2
HC rat3
HC rat4
(b)
Metabolites Count
400
0
338
399
259
114
158
51
49
11
57
5
3
1
Metabolite categories
Organic acids and derivatives
Lipids and lipid-like molecules
Organoheterocyclic compounds
Organic oxygen compounds
Benzenoids
Nucleosides/ nucleotides/ analogues
Organic nitrogen compounds
Alkaloids and derivatives
Phenylpropanoids and polyketides
Organosulfur compounds
Organic 13-dipolar compounds
Organohalogen compounds
(c)
HC
tumor
PC2[14.4%]
PC1[35.2%]
(d)
HC
tumor
t[1]O[9.6%]
t[1]P[36.6%]
(e)
R2Y(cum)
Q2(cum)
Intercepts: R2Y(cum) = (0, 0.92), Q2(cum) = (0, -0.5)
R²Y(cum) and Q²(cum)
Correlation Coefficient
(f)
-log10 (P)
P-value < 0.05
log2(Fold change)
Status
up-regulated (380)
down-regulated (312)
down-regulated
VIP
0.0
1.7
(g)
Relative expression level
-1 -0.5 0 0.5 1
PS(22:4(7Z,10Z,13Z,16Z)/22:6(4Z,7Z,10Z,13Z,16Z,19Z))
N-Acetylaspartic acid
Glucosylceramide_(d18:1/24:1(15Z))
N-Methyl-L-asparagine
PC(22:2)
Val-Asn
Ile-Thr
L-Azetidine-2-carboxylic acid
4-Aminobutyric acid (GABA)
Erythronolactone
Allantoin
2-[[1-(3-Fluorophenyl)imidazol-2-yl]thio]acetic acid
2-amino-3-({hydroxy[2-(icosanoyloxy)-3-(octadecanoyloxy)propoxy]phosphoryl}oxy)propanoic acid
5-methyl-2'-deoxycytidine
Deoxycytidine
4-(3,4-Difluorophenyl)-6,7-dimethyl-3,4-dihydro-2(1H)-quinolinone
1-{2-[(2-Amino-6-hydroxy-9H-purin-9-yl)methoxy]ethoxy}-3-methyl-1-oxo-2-butanamine
PC(35:1)
4-Allyl-3-(4-chlorobenzyl)-1H-1,2,4-triazole-5-thione
PC(20:3(5Z,8Z,11Z)/14:0)
TB rat1
TB rat2
TB rat3
TB rat4
TB rat5
HC rat1
HC rat2
HC rat3
HC rat4

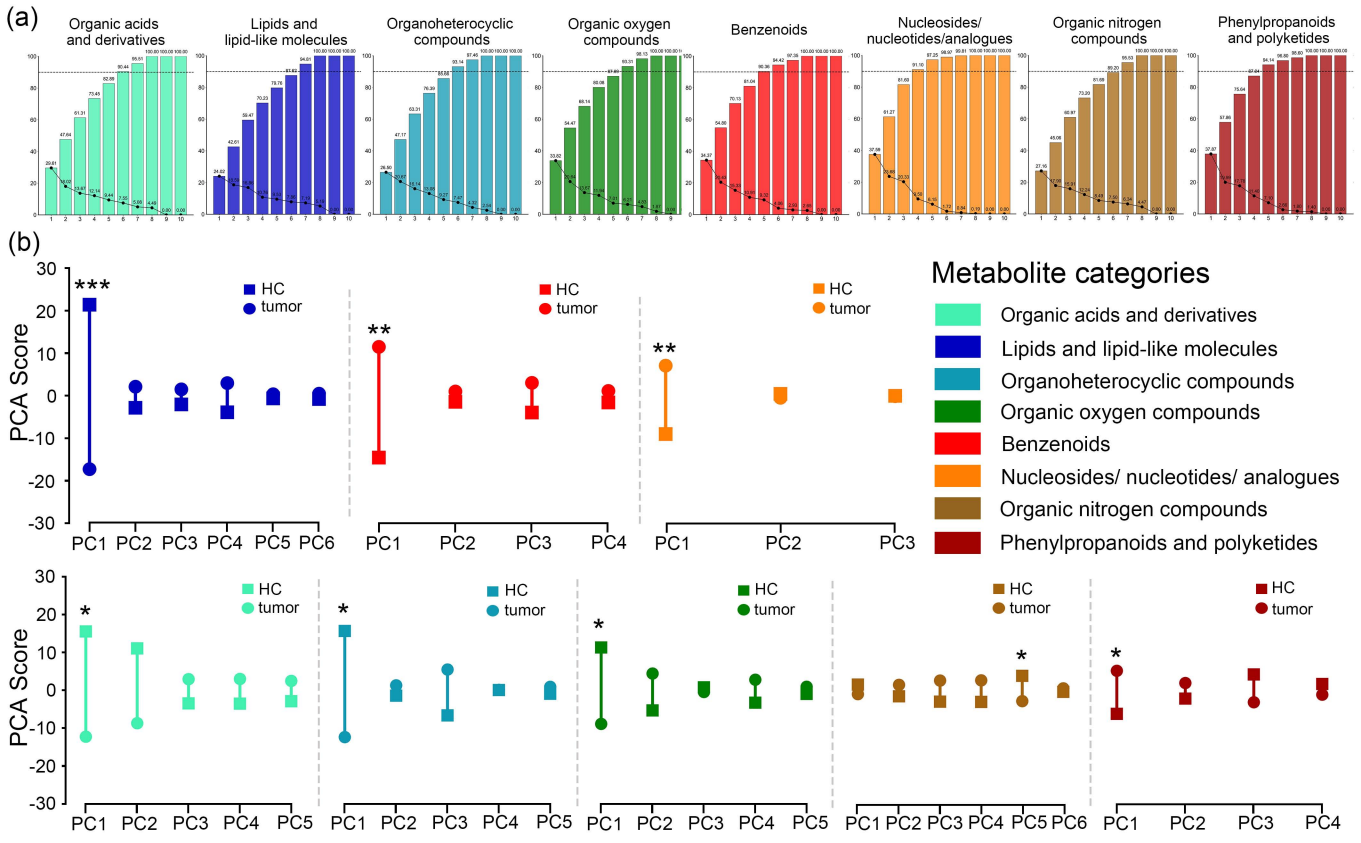
(a)
Organic acids and derivatives
Lipids and lipid-like molecules
Organoheterocyclic compounds
Organic oxygen compounds
Benzenoids
Nucleosides/ nucleotides/analogues
Organic nitrogen compounds
Phenylpropanoids and polyketides
(b)
PCA Score
HC
tumor
PC1 PC2 PC3 PC4 PC5 PC6
Metabolite categories
Organic acids and derivatives
Lipids and lipid-like molecules
Organoheterocyclic compounds
Organic oxygen compounds
Benzenoids
Nucleosides/ nucleotides/ analogues
Organic nitrogen compounds
Phenylpropanoids and polyketides

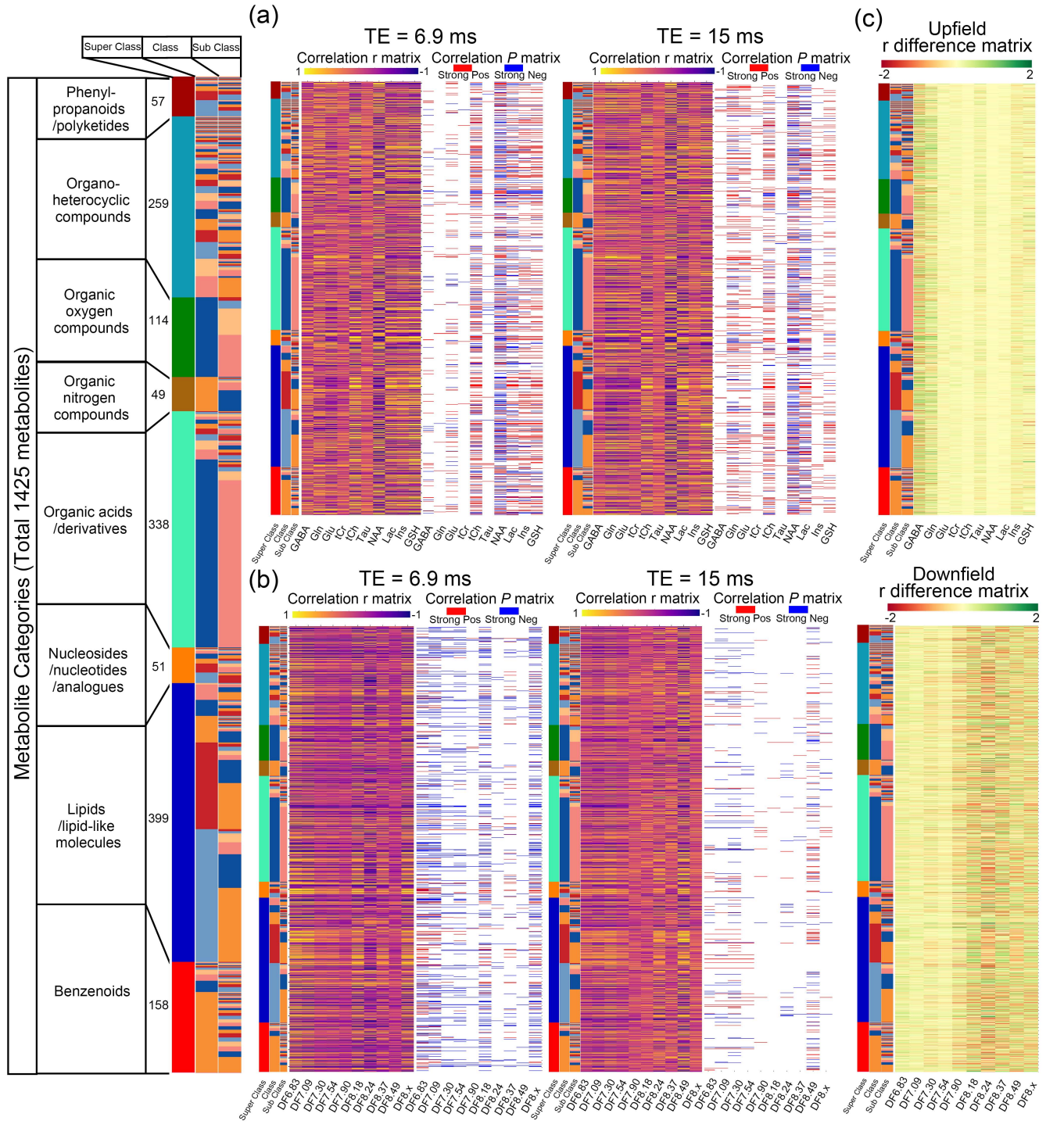
(a)
TE = 6.9 ms
TE = 15 ms
Correlation r matrix
Correlation P matrix
Strong Pos
Strong Neg
(b)
(c)
Upfield
r difference matrix
Downfield
r difference matrix
Super Class
Class
Sub Class
Metabolite Categories (Total 1425 metabolites)
Phenyl-propanoids /polyketides
57
Organo-heterocyclic compounds
259
Organic oxygen compounds
114
Organic nitrogen compounds
49
Organic acids /derivatives
338
Nucleosides /nucleotides /analogues
51
Lipids /lipid-like molecules
399
Benzenoids
158
GABA
Gln
Glu
tCr
tCh
Tau
NAA
Lac
Ins
GSH

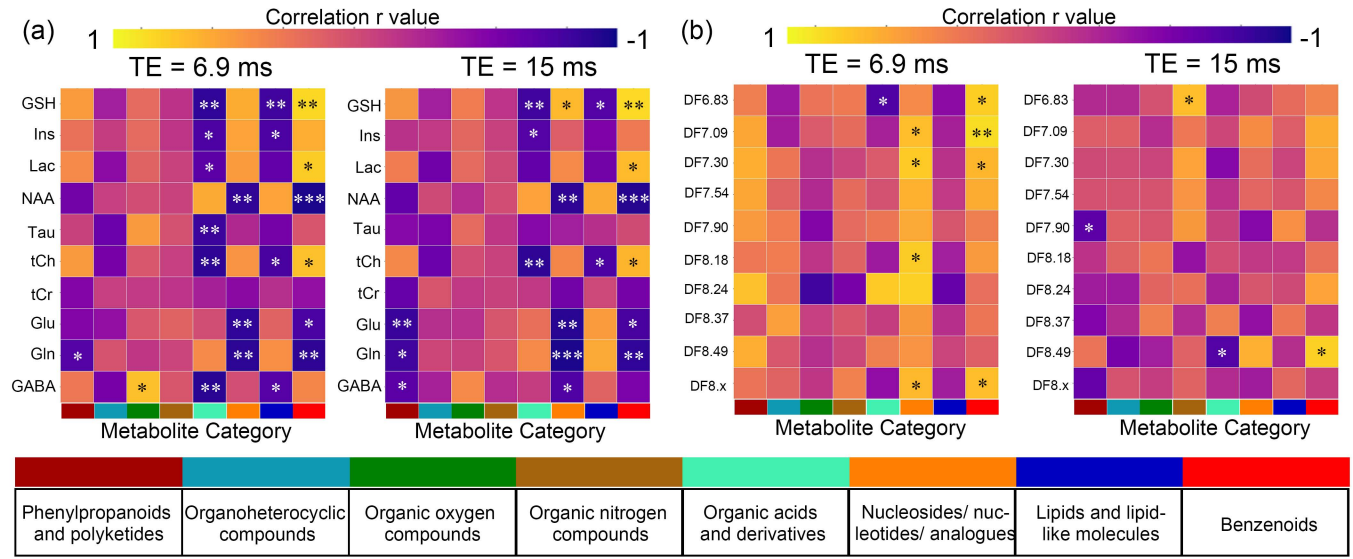
(a)
Correlation r value
1
-1
TE = 6.9 ms
TE = 15 ms
GSH
Ins
Lac
NAA
Tau
tCh
tCr
Glu
Gln
GABA
Metabolite Category
(b)
DF6.83
DF7.09
DF7.30
DF7.54
DF7.90
DF8.18
DF8.24
DF8.37
DF8.49
DF8.x
Phenylpropanoids and polyketides
Organoheterocyclic compounds
Organic oxygen compounds
Organic nitrogen compounds
Organic acids and derivatives
Nucleosides/ nucleotides/ analogues
Lipids and lipid-like molecules
Benzenoids

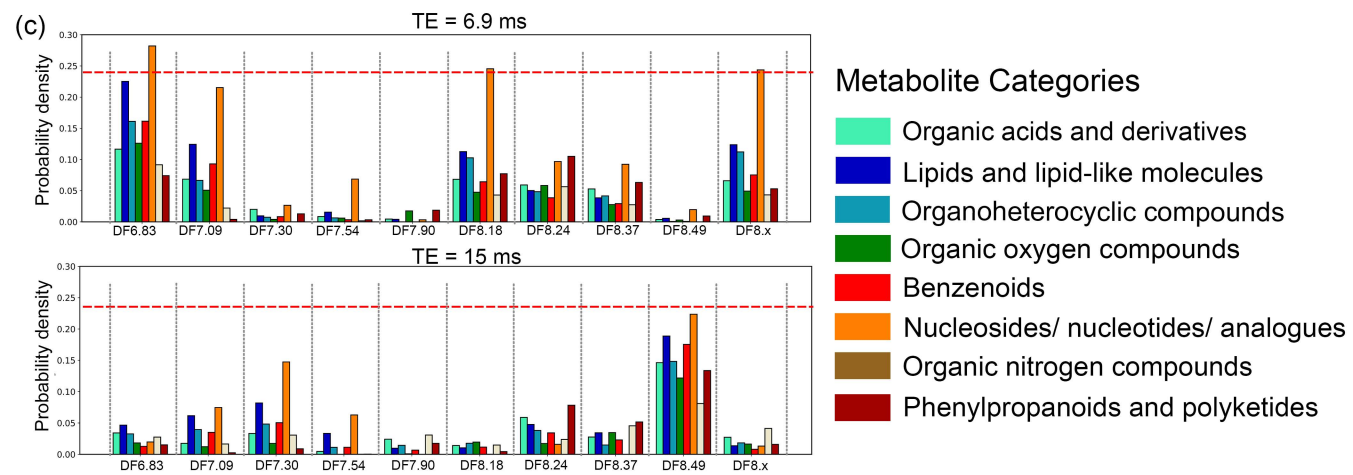
(c)
TE = 6.9 ms
TE = 15 ms
Probability density
DF6.83
DF7.09
DF7.30
DF7.54
DF7.90
DF8.18
DF8.24
DF8.37
DF8.49
DF8.x
Metabolite Categories
Organic acids and derivatives
Lipids and lipid-like molecules
Organoheterocyclic compounds
Organic oxygen compounds
Benzenoids
Nucleosides/ nucleotides/ analogues
Organic nitrogen compounds
Phenylpropanoids and polyketides

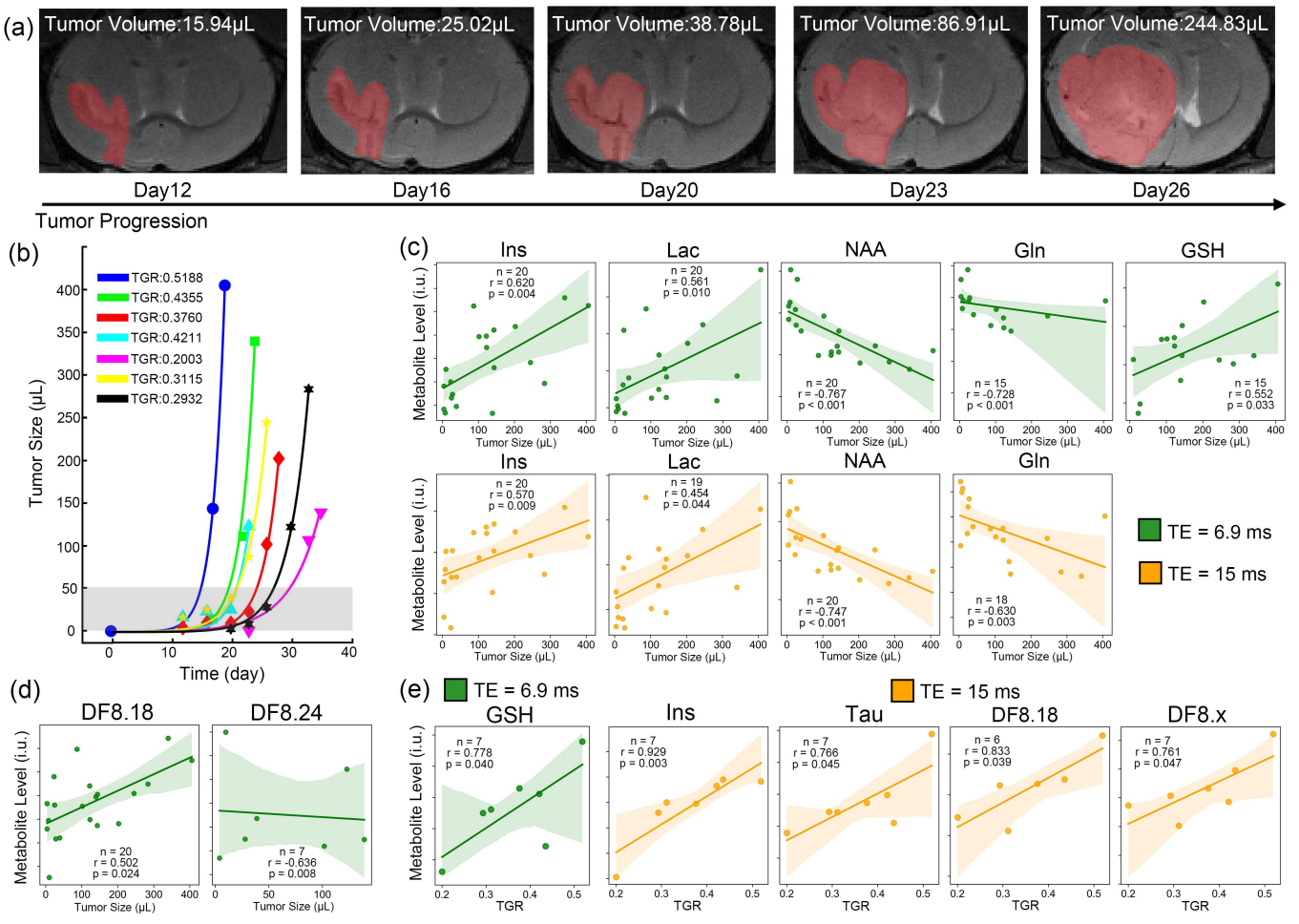
(a)
Tumor Volume:15.94μL
Tumor Volume:25.02μL
Tumor Volume:38.78μL
Tumor Volume:86.91μL
Tumor Volume:244.83μL
Day12
Day16
Day20
Day23
Day26
Tumor Progression
(b)
TGR:0.5188
TGR:0.4355
TGR:0.3760
TGR:0.4211
TGR:0.2003
TGR:0.3115
TGR:0.2932
Tumor Size (μL)
Time (day)
(c)
Ins
Lac
NAA
Gln
GSH
n = 20
r = 0.620
p = 0.004
n = 20
r = 0.561
p = 0.010
n = 20
r = -0.767
p < 0.001
n = 15
r = -0.728
p < 0.001
n = 15
r = 0.552
p = 0.033
n = 20
r = 0.570
p = 0.009
n = 19
r = 0.454
p = 0.044
n = 20
r = -0.747
p < 0.001
n = 18
r = -0.630
p = 0.003
Metabolite Level (i.u.)
Tumor Size (μL)
TE = 6.9 ms
TE = 15 ms
(d)
DF8.18
DF8.24
n = 20
r = 0.502
p = 0.024
n = 7
r = -0.636
p = 0.008
(e)
TE = 6.9 ms
TE = 15 ms
GSH
Ins
Tau
DF8.18
DF8.x
n = 7
r = 0.778
p = 0.040
n = 7
r = 0.929
p = 0.003
n = 7
r = 0.766
p = 0.045
n = 6
r = 0.833
p = 0.039
n = 7
r = 0.761
p = 0.047
TGR